Available online at www.sciencedirect.com
ScienceDirect
Geochimica et Cosmochimica Acta 75 (2011) 119–133
Geochimica et Cosmochimica Acta
www.elsevier.com/locate/gca

Iron solid-phase differentiation along a redox gradient in basaltic soils

Aaron Thompson [a,*], Denis G. Rancourt [b], Oliver A. Chadwick [c], Jon Chorover [d]

[a] Department of Crop and Soil Sciences, University of Georgia, Athens, GA 30602, USA
[b] Formerly at Department of Physics, University of Ottawa, Ottawa, Ont., Canada K1N 5N6
[c] Department of Geography, University of California, Santa Barbara, CA 93106, USA
[d] Department of Soil, Water & Environmental Science, University of Arizona, Tucson, AZ 85721, USA

Received 18 May 2010; accepted in revised form 8 October 2010; available online 15 October 2010

Abstract

Iron compounds in soil are multifunctional, providing physical structure, ion sorption sites, catalytic reaction-centers, and a sink for respiratory electrons. Basaltic soils contain large quantities of iron that reside in different mineral and organic phases depending on their age and redox status. We investigated changes in soil iron concentration and its solid-phase speciation across a single-aged (400 ky) lava flow subjected to a gradient in precipitation (2200–4200 mm yr^{-1}) and hence redox history. With increasing rainfall and decreasing Eh, total Fe decreased from about 25% to <1% of the soil mass. Quantitative speciation of soil solid-phase iron was constrained by combining ^{57}Fe Mössbauer spectroscopy (MBS) at 295 and 4.2 K with powder X-ray diffraction, selective chemical extractions, and magnetic susceptibility measurements. This approach allowed us to partition iron into (1) nanoparticulate and microcrystalline Fe^{III}-(oxy)hydroxides, (2) microcrystalline and bulk Fe^{III}-oxides, (3) organic/silicate bound Fe^{III}, and (4) ferrous iron. The Fe^{III}-(oxy)hydroxide fraction dominated solid-phase Fe, exhibiting a crystallinity continuum based on magnetic ordering temperature. The continuum extended from well-ordered microcrystalline goethite through nanocrystalline Fe^{III}-(oxy)hydroxides to a nano Fe^{III}-(oxy)hydroxide phase of extremely low crystallinity. Magnetic susceptibility was correlated ($R^2 = 0.77$) with Fe^{III}-oxide concentration, consistent with a contribution of maghemite to the otherwise hematite dominated Fe-oxide fraction. The Fe^{III}-(oxy)hydroxide fraction of total Fe decreased with increasing rainfall and was replaced by corresponding increase in the organic/silicate Fe^{III} fraction. The crystallinity of the Fe^{III}-(oxy)hydroxides also decreased with increasing rainfall and leaching, with the most disordered members of the crystallinity continuum, the nano Fe^{III}-(oxy)hydroxides, gaining proportional abundance in the wetter sites. This finding runs counter to the conventional kinetic expectation of preferential removal of the most disordered minerals in a reductive dissolution-dominated environment. We suggest the persistence of highly disordered Fe phases reflects the dynamic redox conditions of these upland soils in which periods of anoxia are marked by high water-throughput and Fe^{2+}(aq) removal, while periodic Fe oxidation events occur in the presence of high concentrations of organic matter. Our ^{57}Fe Mössbauer study shows basalt-derived nano-scale Fe^{III} phases are more disordered than current synthetic analogs and have nano-structural characteristics that are linked to their formation environment.

1. INTRODUCTION

Feedbacks between mineral weathering and ecosystem function affect the rate and trajectory of change in terrestrial biogeochemical systems (Lucas et al., 1993; Torn et al., 1997; Blum et al., 2002; Derry et al., 2005). The implications of this connectivity affect not only present-day contaminant/nutrient dynamics (Genin et al., 2001; Davidson et al., 2003) but can also inform paleoclimatic interpretations of geologic deposits (Yamaguchi et al., 2005). Iron plays a central role in ecosystem function throughout

* Corresponding author. Tel.: +1 706 410 1293.
E-mail address: AaronT@uga.edu (A. Thompson).

0016-7037/$ - see front matter © 2010 Elsevier Ltd. All rights reserved.
doi:10.1016/j.gca.2010.10.005

pedogenesis. Iron oxidation during incongruent weathering of primary minerals results in the formation of secondary Fe phases whose interfacial reactivity exerts strong control over ecosystem cycling of nutrients, carbon, trace elements, and contaminants, including microbial mediation of these processes. The crystal size and bonding environment (collectively termed here "solid-phase speciation") of Fe govern its influence on ecosystem biogeochemistry to a much larger extent than its total abundance. Short-range crystal order and small particle sizes distinguish the most reactive, high surface area Fe components from larger bulk Fe-oxides (Bonneville et al., 2004; Roden, 2006). Fe^{III} cations in these components are typically bonded to oxygen and/or hydroxide anions (i.e., Fe^{III}-oxides vs. Fe^{III}-(oxy)hydroxides) with various amounts of Al^{III} substitution and structural water.

The trajectory of Fe-mineral differentiation depends on environmental redox conditions. Under persistent oxic conditions, the accumulation of secondary Fe(III) minerals is favoured thermodynamically, whereas under anoxic conditions, even well-ordered Fe^{III}-oxide crystals are subjected to reductive dissolution (Bonneville et al., 2004). While thermodynamic data can be effectively employed to predict the stability of iron mineral assemblages under fully oxic or anoxic conditions, the open system and event-based dynamics of soil ecosystems often place them somewhere between these end-member scenarios. Many soils are exposed to variable periods of anoxia, often localized within aggregates and microsites (Sexstone et al., 1985). These redox fluctuations drive local mobilization of Fe^{2+}(aq), which can be either incorporated into ferrous-bearing solids, removed from the soil, or reoxidized and precipitated as Fe^{III}-oxide and -hydroxide surface coatings on ped faces and along preferential flow paths. Little is known regarding the formation and stability of iron phases under these alternating redox conditions, despite the widespread occurrence of such fluctuations in soils. The objective of the present work, therefore, was to examine shifts in iron solid-phase speciation that occur in response to climate-induced redox fluctuations and pedogenic Fe loss across a natural rainfall gradient imposed on soil developed from a single-aged basaltic lava flow.

Moderately weathered Hawaiian soils have high concentrations of organic matter and contain an abundance of short-range-ordered (SRO) iron and alumino-silicate minerals that are typically assessed by selective chemical extractions, infrared spectroscopy and electron microscopy, because they are difficult to detect using standard powder X-ray diffraction (XRD) techniques (Chorover et al., 1999, 2004; Mikutta et al., 2009b). Here, we focus on the Fe-bearing components using ^{57}Fe Mössbauer spectroscopy (MBS) at 295 and 4.2 K, and bulk magnetic susceptibility analysis. MBS is capable of precise physical measurements of Fe nuclear energy levels, which facilitates detection of Fe coordination in SRO minerals. It is inherently a "bulk" spectroscopic technique, requiring >10 mg Fe for detection, and thus is ideal for integrated analysis of whole soil speciation changes.

2. METHODS

2.1. Field area and sampling

The research was conducted on soils collected along a climate gradient situated on the Haleakala Volcano on Maui, HI, where rainfall increases from 2200 to 4200 mm yr^{-1} toward the locus of trade wind interception by the mountain (Miller et al., 2001; Schuur and Matson, 2001). All sites were sampled in undisturbed rain forest. The soils developed in mixed lava and tephra of Kula lava series that was deposited *ca*. 400 ka. We sampled surface A horizons (0–10 cm) and subsurface Bw or Bg horizons (50–70 cm) across this gradient at 2200, 2800, 3500 and 4200 mm yr^{-1} of rainfall, and evaluated a depth sequence at the 3500 mm yr^{-1} site. (Color plates of the soil profiles are shown in Figs. EA-9 and EA-10 of the Electronic Annex.) Soils from the drier two sites were double-bagged in 1.75 mil polyethylene bags with moist paper towels between the layers and placed immediately on ice, according to procedures described in Bartlett and James (1993). For the wetter two sites, soil horizons were classified as either oxic or anoxic based on the presence/absence of redoximorphic features (mottles, gleying, standing water, hydrogen sulfide odor, etc.). Samples considered oxic were treated similarly to soils from the drier sites. Anoxic soils were doubled-bagged in a low O_2-permeable, 3-mil Sarenex inner bag and a 4-mil polyethylene outer bag, flushed three times with ultra-pure N_2, and packed on ice. All soils were transported to the lab on blue ice, homogenized in a 95%:5% N_2:H_2 glove box, frozen at 193 K and then freeze-dried before analysis.

2.2. Notation and definitions

Throughout this work we use the term crystallinity in a broad sense to denote the degree of long-range crystal order. Thus, our use of the terms, poorly-crystalline or nanocrystalline indicate chemical and/or structural deviations from the properties of a perfect bulk crystal structure having ideal end-member composition deriving from any one or combination of the following: a higher degree of vacancy defects, smaller particle size, increased cation substitutions, surface/defect-generated strain fields, electronic-instability defects, etc. A list of abbreviations used in the text is provided in Table 1.

2.3. Analytical approach

Our approach is to use the specificity of ^{57}Fe MBS to expand our understanding of Fe phases that are difficult to detect by standard XRD and selective extraction analyses. To do so we draw on previously published 0.5 M HCl, acid-ammonium oxalate (AAO), and Na-pyrophosphate extractions for these soils (Thompson et al., 2007). In addition, we performed two consecutive citrate-dithionate bicarbonate extractions (Loeppert and Inskeep, 1996) on 0.5 g of dry soil with 30 ml of solution for each step in polypropylene co-polymer centrifuge tubes. Iron from the

Table 1
Less common abbreviations.

General		MBS spectral interpretation	
AAO	Acid-ammonium oxalate	ε	Hyperfine quadrapole splitting
CBD	Citrate–bicarbonate–dithionate	σ_{HFD}	Standard deviation of the HFD
$f_{tot\text{-}Fe}$	Fraction of total Fe	Bhf	Average hyperfine field strength
LHT	Liquid helium temp., 4.2 K	CS	Center shift
MAP	Mean annual precipitation	HFD	Hyperfine field distribution
MBS	Mössbauer spectroscopy	H_{peak}	Most probably hyperfine field strength
MCG	Maui climate gradient	QS	Quadrapole splitting
Na-Pyro	Na-pyrophosphate	QSD	Quadrapole splitting distribution
RT	Room temp., 295 K	T_N	Neel temperature
Fe solid-phases		**MBS spectral assignments**	
Fe^{II}-Ox	Fe^{III}-oxides	LHT-(b)OxHy	Blocked Fe^{III}-OxHy sextet at LHT
Fe^{III}-OxHy	Fe-(oxy)hydroxides	LHT-F	Fe^{II} doublet at LHT
Fe^{II}-$OxHy_{(295\ K)}$	Fe^{III}-OxHy's mag. ordered at 295 K	LHT-Ox	Fe^{III}-oxide sextet at LHT
Fe^{III}-$OxHy_{(4.2–295\ K)}$	Fe^{III}-OxHy's mag. ordered between 4.2 and 295 K	LHT-OxHy	Fe^{III}-OxHy sextet at LHT
Fe^{III}-$OxHy_{(4.2\ K)}$	Fe^{III}-OxHy's mag. ordered below 4.2 K	LHT-Q	Fe^{III} doublet at LHT
Fh	Ferrihydrite	RT-(b)OxHy	Blocked Fe^{III}-OxHy sextet at RT
Gt	Goethite	RT-F	Fe^{II} doublet at RT
Hm	Hematite	RT-Ox	Fe^{III}-oxide sextet at RT
mc-Hm	Microcrystalline hematite	RT-OxHy	Fe^{III}-OxHy sextet at RT
Mh	Maghemite	RT-Q	Fe^{III} doublet at RT
n-Gt	Nano goethite		
SRO	Short-range-ordered		

combined extract solutions was analyzed using inductively coupled plasma-mass spectrometry (Perkin Elmer DRC II ICPMS). Total soil carbon was measured by combustion coupled with CO_2-detection using Shimadzu 5000A-SSM TOC analyzer (Columbia, MD). Fe^{2+} was measured by a revised ferrozine method (Thompson et al., 2006b) following separate 0.5 M HCl extracts conducted on field moist soils at a 1:10 dry soil:solution ratio within a week after field collection.

Soils derived from weathering of basaltic parent materials in tropical environments contain mineral–organic complexes whose speciation and structure can be significantly altered through use of chemical pre-treatments commonly used prior to mineral analysis (Chorover et al., 2004; Mikutta et al., 2009b). We therefore avoided all such pre-treatments and conducted all spectroscopic and diffraction analyses on un-altered bulk samples. While the lack of pre-treatment diminishes the signal-to-noise obtainable by some of the analyses (e.g., XRD), it also better preserves sample integrity and avoids the introduction of artifacts.

2.4. X-ray diffraction (XRD)

2.4.1. XRD collection methods

XRD was conducted on a Philips X'pert MPD powder-sample diffractometer equipped with a spinning stage and X'Celerator multiple strip detector with Ni-filtered CuKα radiation at 45 kV and 40 mA. All samples were scanned from 5 to 75° 2θ, with a step size of 0.017° 2θ and step collection time of 7 s for a total run time of 8 h. Peaks at 2.03 Å are from the sample holder.

2.4.2. XRD interpretation

We identified the principal Fe minerals in the XRD as follows: well-crystallized hematite (Hm) via diffraction lines at d-spacings of 2.70, 2.52, and 1.70 Å; well-crystallized goethite (Gt) via diffraction lines at 4.18, 2.69, and 2.45 Å; and maghemite (Mh) based on a reflection at 2.95 Å (all other lines overlapped with hematite). The short-range ordered Fe^{III}-(oxy)hydroxide phases, ferrihydrite (Fh) and nanocrystalline goethite (n-Gt), are harder to identify in XRD patterns. Both likely exhibit small particle sizes, Fh due to its intrinsic nature (Rancourt and Meunier, 2008; Marchand and Rancourt, 2009), and n-Gt because goethites in tropical basaltic soils are nearly always much smaller than typical synthetic analogs and often highly substituted by Al and other cations (e.g., Ti, Mn, etc.) (Norrish and Taylor, 1961; Langmuir, 1971; Wada and Wada, 1976; Golden et al., 1979; Fey and Dixon, 1981; Murad and Schwertmann, 1983; Fritsch et al., 2005; Waychunas et al., 2005; Otero et al., 2009). It is difficult to separate these two minerals on the basis of their XRD patterns alone. Both have broad reflections and many of those reflections are difficult to resolve from each other in complex mixtures such as soils. For instance, the main 2-line and 6-line Fh broad reflections (1 0 1) at 2.45 Å overlap with broad reflections from the (1 1 2) n-Gt (Cornell and Schwertmann, 2003). Broad (1 1 2) 6-line Fh reflections overlap with broad n-Gt reflections originating from the (4 0 1) and (2 1 1) orientations at 2.2 Å. Similarly, the broad (1 1 4) Fh reflection at 1.7 Å overlaps with the broad (2 1 2) reflection of n-Gt and in these soils may also be obscured by broad reflections from the kaolin-group minerals at 1.7 Å. Similarly the 1.5 Å (3 0 0) Fh line overlaps with these

kaolin-group minerals, which are present in many samples. Thus, the best diagnostic peaks are the broad (1 0 1) peak of n-Gt at 4.18 Å and the broad 6-line Fh reflection (1 1 3) at 1.96 Å. Since the broad (1 0 1) n-Gt peak is the largest Gt reflection, we expect it in all samples containing goethite. Likewise, we expect samples with Fh to exhibit a main peak at ~2.45 Å, however since this overlaps with a prominent n-Gt reflection of only slightly smaller intensity than the 4.18 Å n-Gt reflection, we must further inspect the 1.96 Å region for the smaller (1 1 3) Fh reflections to establish an XRD signal for Fh.

2.5. Magnetic susceptibility

Mass-specific magnetic susceptibility (MS) measurements were collected on freeze-dried soils at 295 K in a custom-built AC-susceptibility bridge at the University of Georgia. Measurements were cross calibrated by Dr. Christoph Geiss (Trincoll University) on a KLY-4 Kappabridge susceptibility bridge (ASC Scientific).

2.6. ^{57}Fe Mössbauer spectroscopy

2.6.1. MBS collection and analysis methods

All LHT and RT ^{57}Fe Mössbauer spectra were collected in transmission mode using a 10–50 mCi ^{57}Co-Rh source kept at RT. Freeze-dried powder samples were mounted in holders with 1.27 cm diameter windows and a thickness up to 0.64 cm (~100–500 mg per holder) based on the ideal absorber thickness calculated on the basis of bulk elemental composition to optimize signal-to-noise (Rancourt et al., 1993). The RT measurements had data accumulation times of 1–2 wks, whereas collection time was limited in the cryogenic measurements (by labor and cryogen costs) to approximately 1 d.

All measurements were performed with a velocity range of ± 11 mm s^{-1} and achieved the typical detection limit of 0.1–1% of Fe. Velocity (i.e., gamma-ray energy) was calibrated using an enriched ^{57}Fe foil at 298 K and all center shifts (CSs) and peak positions are reported with respect to this standard. The transducer was operated in constant acceleration mode and folding was performed to achieve a flat background. The spectra were not corrected for thickness effects (Rancourt et al., 1993). Cryogenic measurements were performed in a shielded, He gas flow type cryostat with temperature monitoring at the He gas outflow port and on the sample holder mount. The temperature during data collection did not rise above 4.5 K. Using this setup, temperature gradients across the absorber dimensions are typically less than 0.1 K per 1/2 inch. The entire setup is vibration isolated and calibration tests showed less than 0.001 mm s^{-1} peak-width broadening on standards.

2.6.2. MBS spectral analysis approach

Mössbauer spectral fitting of all the RT and LHT spectra was performed using the Voigt-based fitting (VBF) method of Rancourt and Ping (1991) for quadrupole splitting distributions (QSDs) and combined hyperfine field distributions (HFDs), as implemented in the Recoil™ software, developed by Rancourt in collaboration with ISA Inc. (http://www.isapps.ca/recoil). All VBF Mössbauer parameter definitions and a description of the relevant notation are given by Rancourt and Ping (1991). All errors in Mössbauer fitting parameters are two-standard deviation (2σ) errors, as calculated by Recoil™. In reporting quantitative phase abundances or site populations it is assumed that the Mössbauer recoilless fractions of all detected phases or Fe-bearing components are equal, such that subspectral areas (expressed as fractions of total spectral area) are equal to the amounts of Fe (expressed as fractions of total Fe) in the corresponding phases or components. This assumption is expected to be valid at cryogenic temperatures, and also to be a good approximation at RT with dry samples (Lalonde et al., 1998; Rancourt, 1998).

Details regarding the fitting approach and explanations of key MBS parameters are contained in Section EA-1 of the Electronic Annex. Briefly, we fit all paired 295 and 4.2 K spectra with a spectral component model in which the components could be assigned to four broad Fe bonding environments: (a) Fe^{III}-(oxy)hydroxides (Fe^{III}-OxHy); (b) Fe^{III}-oxides (Fe^{III}-Ox); (c) organic/silicate bound Fe^{III}; and (d) paramagnetic ferrous iron species (no magnetite octets were detected). We further divided the Fe^{III}-OxHy assignment into three size/crystallinity categories based on the temperature of magnetic ordering (T_N): (a_1) <4.2 K (Fe^{III}-$OxHy_{(<4.2\ K)}$); (a_2) 4.2–295 K (Fe^{III}-$OxHy_{(4.2–295\ K)}$); (a_3) >295 K (Fe^{III}-$OxHy_{(>295\ K)}$). While the fitting error is small between the four broad groups, there are trade-off uncertainties between the sub-groups of the Fe^{III}-OxHy assignment.

3. RESULTS

Prior work (Miller et al., 2001; Schuur and Matson, 2001; Thompson et al., 2007) along the Maui climate gradient (MCG) gradient confirmed a negative correlation between total Fe and a greater frequency of "suboxic" and "anoxic" Eh values with increasing rainfall (Fig. 1). These data reveal that total Fe decreases from >25% of dry soil mass at low rainfall to <1% at the highest rainfall site (Table 2).

3.1. Selective chemical extractions

Prior chemical extraction data from Thompson et al. (2007) are summarized in Table 2 along with new data for CBD extractable Fe and total C. In the surface horizons the fraction of total Fe ($f_{tot\text{-}Fe}$) extracted by HCl, oxalate (AAO), and Na-pyrophosphate (Na-Pyro) all increase with increasing rainfall, whereas the CBD-extractable $f_{tot\text{-}Fe}$ (0.46 ± 0.06) is similar at all sites. In the subsurface horizons, increasing rainfall drives a decrease in the $f_{tot\text{-}Fe}$ extracted by AAO, Na-Pyro, and CBD (Table 2). At the 3500 mm yr^{-1} site the $f_{tot\text{-}Fe}$ extracted by all treatments decreased with depth. As a function of increasing rainfall, total carbon increased in the surface horizons and decreased in the subsurface horizons and with depth at the 3500 mm yr^{-1} site. Increasing rainfall also increases the HCl-extractable Fe^{2+} $f_{tot\text{-}Fe}$.

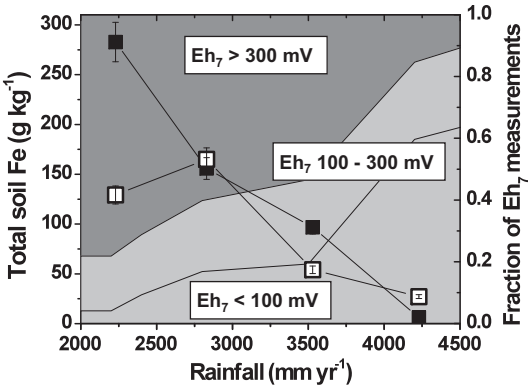

Fig. 1. Iron (Fe) and redox (Eh) changes across the Maui climate gradient. Open and closed squares indicate total soil Fe for the subsurface and surface transects, respectively. Error bars give one SD based on triplicate analysis of a single sample (Thompson et al., 2007). Long-term average redox potential measurements (360 pt electrode measurements taken every 6 wks from 15 cm, 35 cm, and 50 cm depths over 18 mo) from Schuur and Matson, 2001 are binned in three categories redox categories: Oxic (dark shading) = Eh7 > 300 mV; suboxic (medium grey shading) = 100 mV < Eh7 > 300 mV; anoxic (white) = Eh7 < 100 mV.

3.2. Analysis of X-ray diffraction data

Positive XRD peak identification has been made for the following minerals in various proportions throughout the sample set: quartz, muscovite, hematite, goethite, a short-range-ordered kaolin-group mineral (e.g., kaolinite/halloysite), anatase and illmenite. Well-crystallized hematite was identified in six samples: the surface and subsurface samples from 2200 to 2800 mm yr^{-1} sites; the surface 3200 mm yr^{-1} site; and the 58–85 cm depth sample from the 3200 mm yr^{-1} site (Figs. EA-2, EA-3, and EA-4 of the Electronic Annex). Well-crystallized goethite was identified in three samples: the subsurface site 3200; and the surface and subsurface of site 2800 mm yr^{-1}. Evidence for maghemite is present in five soils: all surface soils, except the 4200 mm yr^{-1} site; and at depth in the 2200 and 3500 mm yr^{-1} sites (Figs. EA-2, EA-3 and EA-4 of the Electronic Annex). Our XRD analysis yields supporting evidence for nano-geothite in all samples except the 4200 site and weak suggestions of ferrihydrite in all other samples except the 2200 mm yr^{-1} site and the surface of the 4200 mm yr^{-1} site.

3.3. Field variation in Mössbauer-assigned Fe phase abundance

Below we detail the change in Mössbauer-assigned abundance of Fe solid phases across the climate gradient. The molecular-level characteristics of these Fe solid phases revealed by Mössbauer spectroscopy are included in Section 4, immediately before the discussion section.

In both the surface and subsurface transects, increasing rainfall from 2800 to 4200 mm y^{-1} results in a proportional decrease in the soil Fe^{III}-(oxy)hydroxide $f_{tot\text{-}Fe}$ coincident with a proportional increase in ferrous and organic/silicate $f_{tot\text{-}Fe}$, while $f_{tot\text{-}Fe}$ assigned to the Fe^{III}-oxides shows a variable climatic response (Fig. 2). Solid-phase ferrous iron, detectable only at the higher rainfall sites, never exceeds 5% of the total soil iron pool. Thus, Fe(III) is predominant even when mean Eh values would predict a prevalence of Fe(II) (see Fig. 1). Generally, only a small fraction of the Fe^{III}-OxHy ordered at 295 K and could be identified as

Table 2
Fe concentrations from selective extractions, magnetic susceptibility and total organic carbon for the Maui climate gradient samples.

Horizon	Total Fe[a]	Fe from selective (non-sequential) extractions (g kg^{-1} soil)					Mag. Sus. χ (10^{-8} m^3 kg^{-1})	TOC (g kg^{-1})
		HCl[a]	Na-Pyro[a]	Oxalate[a]	HCl (Fe^{II})[c]	CBD		
Surface (10–20 cm)								
2200 mm (A)	283.0 (198)[b]	24.8 (14)	108.9 (83)	59.0 (34)	0.7 (1)	122.1 (75)	3714 (29)	108 (4)
2800 mm (A)	156.0 (109)	16.0 (46)	64.2 (16)	38.6 (5)	0.5 (1)	64.7 (15)	1404 (36)	218 (2)
3500 mm (Ag)	97.0 (68)	27.7 (16)	33.8 (26)	41.5 (25)	0.2 (1)	44.6 (40)	919 (41)	107 (3)
4200 mm (A)	6.2 (4)	1.8 (1)	3.9 (2)	5.3 (4)	0.5 (4)	3.3 (5)	32 (17)	478 (5)
Subsurface (50–70 cm)								
2200 mm (Bw3)	129.4 (91)	17.0 (26)	46.8 (5)	38.4 (5)	1.4 (4)	57.0 (76)	1438 (105)	130 (2)
2800 mm (Bw3)	165.1 (116)	5.0 (5)	75.9 (41)	42.4 (72)	0.5 (1)	98.3 (24)	163 (19)	87 (1)
3500 mm (Bw3)	54.3 (38)	1.6 (1)	11.3 (10)	10.0 (14)	0.3 (1)	15.1 (21)	510 (138)	83 (6)
4200 mm (Bg3)	27.3 (19)	0.5 (0)	2.6 (12)	2.1 (0)	0.5 (0)	2.6 (4)	31 (16)	49 (1)
Depth profile (3500 mm MAP)								
6–13 cm (Ag)	97.0 (68)	27.7 (16)	33.8 (26)	41.5 (25)	0.2 (1)	44.6 (40)	919 (41)	107 (3)
13–23 cm (Bw1)	76.0 (53)	8.3 (13)	41.8 (18)	34.5 (13)	0.5 (0)	35.8 (74)	224 (21)	128 (2)
40–58 cm (Bw3)	54.3 (38)	1.6 (1)	11.3 (10)	10.0 (14)	0.3 (1)	15.1 (21)	510 (138)	83 (6)
58–85 cm (Bw4)	66.5 (47)	1.6 (0)	3.0 (8)	6.0 (10)	0.2 (1)	15.8 (15)	1744 (68)	89 (1)

[a] Data reprinted from Thompson et al. (2007). Extractions done with soil:solution ratio of 1:60.

[b] Errors are 1 standard deviation (1σ) based on: (a) triplicate analysis of a single sample for total Fe; (b) three replicates of the selective extractons and carbon data; (c) 15 replicates of the magnetic susceptibility data. Uncertainty is presented as the error in the last digit in concise notation (e.g., 5.0 (15) = 5.0 ± 1.5).

[c] Data from a separate 0.5 M HCl extraction with a soil:solution ratio of 1:10.

microcrystalline goethite, while the majority ordered at 4.2 K (Fe^{III}-$OxHy_{(4.2–295\ K)}$) or below (Fe^{III}-$OxHy_{(4.2\ K)}$). The ordering-temperature based subdivision of the Fe^{III}-OxHy class suggests that the mean particle size/crystallinity decreases with increasing rainfall. The Fe^{III}-$OxHy_{(<4.2\ K)}$ sub-class increases as a fraction of the total Fe^{III}-OxHy with increasing rainfall in both the surface and subsurface horizon transects. This is most notable in the surface horizons in which at the highest rainfall site, none of the Fe^{III}-OxHy were ordered at room temperature (i.e., no Fe^{III}-$OxHy_{(>295\ K)}$ detected).

With depth, the $f_{tot\text{-}Fe}$ of each phase was variable and did not exhibit significant trends with the exception that surface horizons contained proportionally more Fe^{III}-organic/silicate and nano-Fe^{III}-(oxy)hydroxides (Fe^{III}-$OxHy_{(4.2\ K)}$), while the subsurface horizons contained more Fe^{III}-oxides. These trends are evident within the four-sample depth profile at the 3500 mm yr^{-1} site (Fig. 3) and also generally reflected in the surface and subsurface transects (Fig. 2).

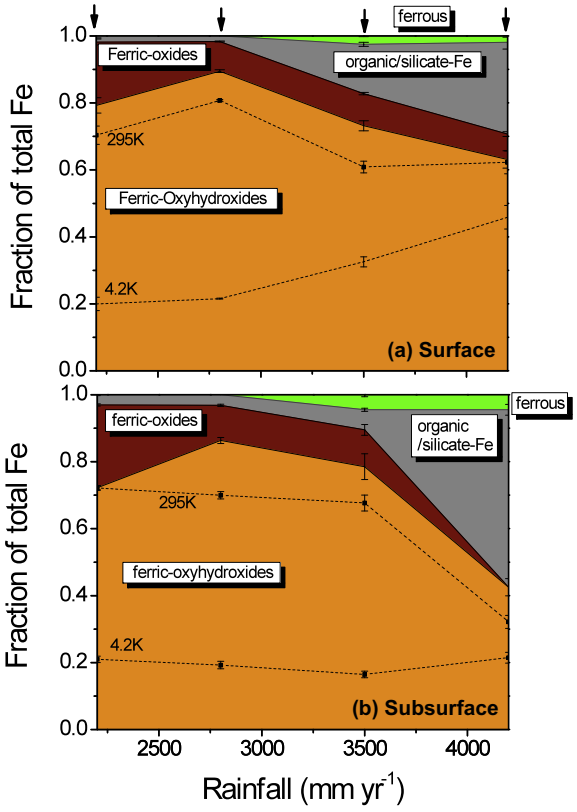

Fig. 2. ^{57}Fe Mössbauer modeled Fe distribution for a surface (a) and subsurface (b) transect across the MCG. The fraction of four broad Fe-bearing group assignments was calculated from the proportional spectra area of the MBS-modeled components (see Tables 3 and 4, Fig. 4, and the Figs. EA-5 and EA-6 of the Electronic Annex) as follows: ferrous (green) = RT-F; organic/silicate-Fe (grey) = RT-Q; Fe^{III}-oxides (red) = RT-Ox; Fe^{III}-(oxy)hydroxides (orange) = LHT-OxHy + LHT-(b)OxHy. The Fe^{III}-(oxy)hydroxide (orange) assignment is split across a crystallinity continuum into three fractions based on MBS-ordering temperature with fraction of the most crystalline end-member (RT-HyOx) shown above the 295 K line and that of the least crystalline end-member (LHT-(b)OxHy) below the 4.2 K line. Errors are 2σ, calculated using the covariance matrix in Recoil. (For interpretation of the references to color in this figure legend, the reader is referred to the web version of this article.)

4. MÖSSBAUER PHASE ANALYSIS

Details regarding the fitting of the spectral components and how these relate to the identified Fe phases are contained in Section 1 of the Electronic Annex. Below we provide an analysis of the four broad Fe populations.

4.1. Fe^{III}-(oxy)hydroxide populations

Synthesis of the RT and LHT MBS spectra suggests the Fe^{III}-(oxy)hydroxide solid phases in these soils exhibit a continuum of crystallinities. Those at the more crystalline end are recognized as microcrystalline-goethites that order at RT (Figs. 4 and EA-5, EA-6, and EA-7 of the Electronic Annex). These are best developed in the 2800 mm yr^{-1} site, where strong XRD reflections of goethite are present at 4.18 Å along with lower intensity peaks at 2.69 and 2.45 Å d-spacing (Figs. EA-2 and EA-3 of the Electronic Annex). These phases (Fe^{III}-$OxHy_{(295\ K)}$) exhibit lower field strengths (Bhf_{RT} ~35T vs. 38T for pure goethite), higher RT CS values (CS ~0.42 mm s^{-1} vs. CS ~0.37 for pure goethite) and less negative quadrapole splitting ($\varepsilon = -0.06$ to -0.14 vs $\varepsilon \sim -0.26$ for pure goethite) than pure goethite (Table 4). This is consistent with a lower crystalline character that likely derives from some combination of Al substitution and reduced particle size. Both factors have been shown to reduce Bhf by as much as 6T in synthetic samples (Goodman and Lewis, 1981); synthetic and natural Al-substituted goethites also typically have higher CS and less

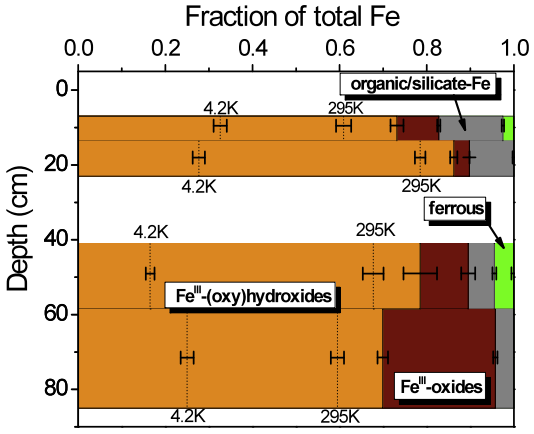

Fig. 3. ^{57}Fe Mössbauer modeled Fe distribution along the depth gradient at the 3500 mm yr^{-1} site. The fraction of four broad Fe-bearing group assignments was calculated from the proportional spectra area of the MBS-modeled components (see Tables 3 and 4, and Fig. EA-7 of the Electronic Annex) as described in Fig. 2. Errors are 2σ, calculated using the covariance matrix in Recoil. (For interpretation of the references to color in this figure legend, the reader is referred to the web version of this article.)

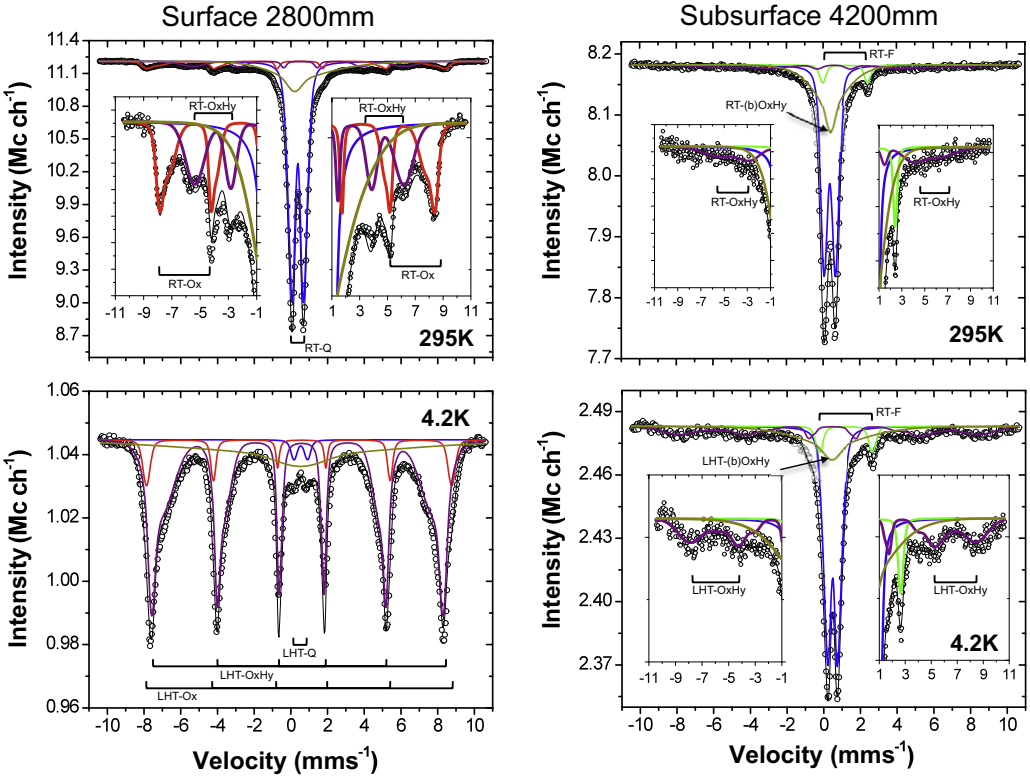

Fig. 4. Fitted ^{57}Fe Mössbauer spectra of (a) surface 2800 mm yr^{-1} and (b) subsurface 4200 mm yr^{-1} at 295 and 4.2 K. The black solid line is the total calculated fit, through the discrete data points (circles). The high and low velocity wings are shown as insets when possible. The resolved spectral components at 295 K are: (1) RT-Q, the dominant doublet (blue line); (2) RT-Ox, the wide sextet (red line); (3) RT-OxHy, a broadened sextet (purple line); and (4) RT-(b)OxHy, a highly broadened (collapsed sextet) central contribution (yellow line); (5) RT-F, a doublet corresponding to ferrous iron. The resolved spectral components at 4.2 K are: (1) LHT-Q, a doublet giving rise to the two shallow central peaks (blue line); (2) LHT-Ox, a wide sextet contributing to the outermost peaks that is equal in area, within error, to RT-Ox (red line); (3) LHT-OxHy, corresponding to the dominant (i.e., deepest peaks) sextet (purple line); and (4) LHT-(b)OxHy, a collapsed 'sextet' (yellow line); (5) RT-F, a doublet corresponding to ferrous iron. (For interpretation of the references to color in this figure legend, the reader is referred to the web version of this article.)

negative quadrapole splitting than pure goethites (Goodman and Lewis, 1981; Kukkadapu et al., 2001; Vandenberghe et al., 2000).

In the middle of the Fe^{III}-OxHy crystallinity continuum, are the LHT-ordered sextets (Fe^{III}-OxHy$_{(4.2–295\ K)}$). A plot of the quadrapole splitting (ε) vs. the most probable hyperfine field (H_{peak}) for these sextets illustrates they have lower H_{peak} than typical nano-goethite (n-Gt) standards, yet more negative ε values than a set of un-substituted and As-substituted ferrihydrite (Fh) standards (Fig. 5). The quadrapole splitting parameter (ε) is a sensitive measure of electron asymmetry, which is strongly influenced by lattice structure in ferric phases. Thus, Fh, which has inherent high structural disorder (Marchand and Rancourt, 2009) and very little mineral averaged asymmetry, will always exhibit ε values close to zero (Mikutta et al., 2008). In contrast, Gt with its needle-like character will have a higher degree of asymmetry and more negative ε values. In most of our samples, the more negative ε values suggest a strong n-Gt contribution (Fig. 5a). However, several of our samples have ε values that approach those of Fh, with one sample (surface 4200 mm yr^{-1} site) containing high organic matter (48%) and low Fe (0.6%) in which ε is very poorly constrained and gives equally acceptable fits across the Fh to n-Gt parameter region (Fig. 5a). Variation in crystallinity within a mineral phase often produces co-variation in the sextet line broadening (σ_{HFD}) and hyperfine field strength (Bhf) along a phase specific slope as illustrated in Fig. 5b for n-Gt and Fh (Van Der Zee et al., 2003). Our samples generally have smaller line widths and/or lower Bhf values than expected for the n-Gt slope in Fig. 5b. This also suggests an admixture of Fh within these soils or perhaps that certain types of disorder affect Bhf and σ_{HFD} differently. It is also plausible for most of the magnetic domains of individual Fe^{III}-OxHy minerals to exhibit lattice asymmetry consistent with typical n-Gt, while other domains within these minerals partially lose this asymmetry and exhibit ε values closer to synthetic, cation-substituted Fh.

At the most disordered end of the crystallinity continuum, are the collapsed sextets at 4.2 K (LHT-(b)OxHy), which are assigned to nano-Fe^{III}-(oxy)hydroxides (Fe^{III}-OxHy$_{(<4.2\ K)}$) near their ordering temperature (T_N). These phases represent a unique feature of these Hawaiian soils and are discussed more completely in the discussion.

Table 3
Fe concentrations[a] (g kg^{-1} dry soil) from Mössbauer spectroscopy (MBS).

Horizon	Mössbauer-determined Fe concentrations					
	Fe-oxides	Fe-oxyhydroxides			Organic/silicate Fe	Ferrous-Fe
		RT ordered	LHT ordered	Un-ordered		
Surface (10–20 cm)						
2200 mm (A)[b]	53.5 (45)[c]	41.3 (51)	142.6 (126)	56.6 (69)	5.1 (16)	N.D.
2800 mm (A)	13.8 (10)	13.2 (10)	92.3 (65)	33.7 (24)	2.6 (4)	N.D.
3500 mm (Ag)	9.3 (7)	17.3 (14)	27.4 (26)	31.6 (27)	14.3 (12)	2.5 (3)
4200 mm (A)	0.5 (1)	N.D.[b]	1.0 (2)	2.9 (3)	1.7 (2)	0.1 (0)
Subsurface (50–70 cm)						
2200 mm (Bw3)	32.0 (23)	N.D.	69.4 (50)	27.2 (23)	4.0 (4)	N.D.
2800 mm (Bw3)	17.4 (13)	28.9 (22)	83.8 (62)	31.9 (29)	5.2 (6)	N.D.
3500 mm (Bw3)	6.0 (10)	6.5 (13)	27.8 (23)	9.0 (8)	3.3 (3)	2.4 (4)
4200 mm (Bg3)	N.D.	2.4 (0)	2.9 (6)	5.9 (6)	14.5 (11)	1.3 (1)
Depth profile (3500 mm MAP)						
6–13 cm (Ag)	9.3 (7)	17.3 (14)	27.4 (26)	31.6 (27)	14.3 (12)	2.5 (3)
13–23 cm (Bw1)	2.7 (2)	5.8 (4)	38.6 (28)	21.1 (18)	7.8 (6)	N.D.
40–58 cm (Bw3)	6.0 (10)	6.5 (13)	27.8 (23)	9.0 (8)	3.3 (3)	2.4 (4)
58–85 cm (Bw4)	17.2 (13)	10.2 (9)	22.9 (19)	16.6 (15)	2.8 (3)	N.D.

[a] Concentrations are calculated by multiplying the fraction of spectral area for each phase in the MBS by the total Fe (see Table 2).
[b] N.D., none detected.
[c] Errors are propagated from 2σ errors calculated in Recoil for the MBS and 1σ errors of total Fe. Uncertainty is presented as the error in the last digit in concise notation (e.g., 5.0 (15) = 5.0 ± 1.5).

Table 4
Descriptions of the MBS components and assignment to solid phases.

Component label		Spectral shape	Assignment	MBS parameter ranges		
				CS (mm s^{-1})[a]	QS or ε (mm s^{-1})	Bhf (T)
Room temp. (RT) spectra						
RT-Q	(blue)	Doublet (central)	Org./silicate Fe^{III} and Fe^{III}-OxHy (<295 K)	0.36 to 0.39	0.62 to 0.90	n/a
RT-F	(green)	Doublet (high-energy)	Ferrous Fe	1.04 to 1.20	0.8 to 2.5	n/a
RT-Ox	(red)	Sextet (widest)	Fe^{III}-oxides (Hm/Mh)	0.33 to 0.38	−0.03 to −0.13	47.1 to 49.8
RT-OxHy	(purple)	Sextet (middle)	Fe^{III}-OxHy (>295 K)	0.40 to 0.64	−0.06 to −0.29	31.7 to 36.9
RT-(b)OxHy	(yellow)	Sextet (collapsed)	Fe^{m}-OxHy (<295 K)	0.32 to 0.69	0.0 to 0.50	0.0 to 27.0
Liq. He Temp. (LHT) spectra						
LHT-Q	(blue)	Doublet (central)	Org./silicate Fe^{III}	0.47 to 0.54	0.68 to 0.82	n/a
LHT-F	(green)	Doublet (high)	Ferrous Fe	1.15 to 1.51	2.3 to 3.1	n/a
LHT-Ox	(red)	Sextet (widest)	Fe^{III}-oxides (Hm/Mh)	0.44 to 0.53	0.00 to −0.11	51.1 to 52.6
LHT-OxHy	(purple)	Sextet (middle)	Fe^{III}-OxHy (4.2–295 K)	0.37 to 0.50	−0.08 to −0.14	46.3 to 48.5
LHT-(b)OxHy	(yellow)	Sextet (collasped)	Fe^{III}-OxHy (<4.2 K)	0.41 to 0.94	0.0 to 0.45	12.7 to 39.6

[a] All CS values are given relative to α-Fe at 295 K.

4.2. Fe^{III}-silicate/organic-bound Fe populations

Fe atoms in silicates and monomeric organic complexes are too distant from each other to order magnetically, and thus both site populations produce a doublet at LHT with CS (median 0.50 mm s^{-1}) and QS (median 0.75 mm s^{-1}) values consistent with octahedrally coordinated, trivalent Fe (Table 4). In most of our samples, the LHT doublet is a minor component of the spectra, however in the 4200 mm yr^{-1} site samples it is the dominant feature (Figs. 4, EA-5 and EA-6 of the Electronic Annex). Here small differences in the LHT-Q components for the surface and subsurface 4200 mm yr^{-1} site soils are consistent with an assignment of organic-Fe^{III} complexes in the surface horizons and isomorphic substitution of Fe^{III} in silicates in the subsurface soils. The carbon-rich (480 g kg^{-1}) surface soil has a CS value of 0.53 mm s^{-1}, which is close to LHT CS values of 0.54 mm s^{-1} for organically-complexed Fe in peat soils reported by Schwertmann and Murad (1988). Whereas, the kaolinite/halloysite-rich subsurface soil has a CS of 0.48 mm s^{-1}, which is similar to that of 0.47–0.49 mm s^{-1} reported for kaolin-group minerals by Fysh et al. (1983). The small size of the doublets at all other sites preclude extension of this analysis to the rest of the samples.

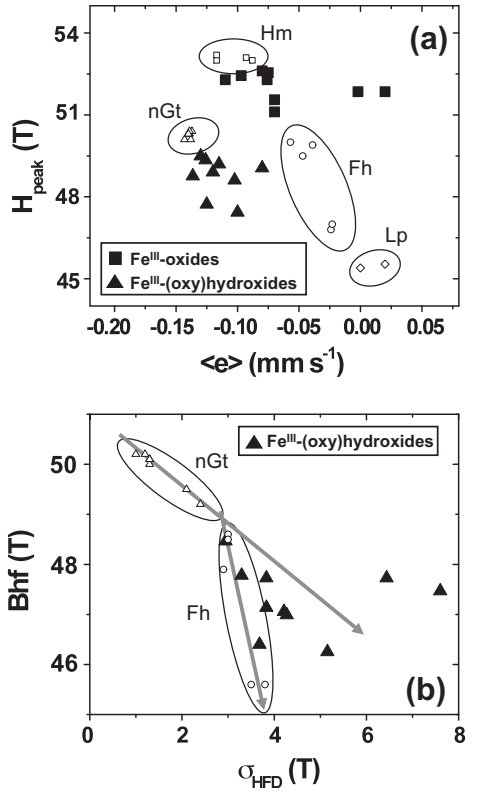

Fig. 5. Hyperfine parameters from liquid helium sextets (LHT-Ox and LHT-OxHy) of all soils sampled and reference oxides and (oxy)hydroxides. (a) Most probable hyperfine field, H_{peak}, vs. average quadrupole shift, ε, in soil samples and reference materials from Van der Zee et al. (2003) (Fh, ferrihydrites; Gt, goethites;, Hm, hematites;, Lp, lepidocrosites). (b) Average hyperfine field, Bhf, vs. σ_{HFD}, which is a measure of line width, for the soil and reference ferrihydrites and goethites. The arrows indicate the trend in the reference Fh's and Gt's from higher to lower crystallinity.

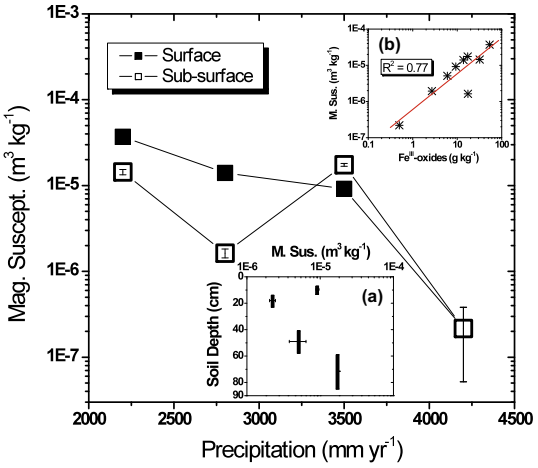

Fig. 6. Bulk magnetic susceptibility (295 K) as a function of rainfall for the surface and subsurface transects (main panel). Inset (a) magnetic susceptibility along the depth gradient at the 3500 mm yr^{-1} site. Inset (b) Log–Log plot of magnetic susceptibility vs. Fe^{III}-oxide concentration calculated from MBS (see Table 3) for all soil samples.

4.3. Paramagnetic ferrous populations

The ferrous doublet components in our samples are best resolved in the higher resolution RT spectra. We observe paramagnetic ferrous contributions in four samples at the higher end of the rainfall gradient with RT QSD's falling into three distinct identity groups consistent with (1) ilmenite (surface 3500 mm yr^{-1}), (2) pyroxenes (subsurface 3500 mm yr^{-1}), and (3) sheet silicates or sorbed Fe^{2+} (both depths at 4200 mm yr^{-1}, see Fig. 4). No octets consistent with the presence of magnetite were observed in any of the spectra. The position of the high-energy line at 1.4 mm s^{-1} is diagnostic for ilmenite. The high-energy lines (H_L) at 2.42 mm s^{-1} in the 4200 mm yr^{-1} site are much too high for ilmenite and are consistent with those commonly reported for alumino-silicate clays (Murad and Cashion, 2004), especially those of kaolinite for which H_L averages 2.4 ± 0.1 mm s^{-1} based on a compilation of eight studies reporting Fe^{II} in kaolinites (Murad and Cashion, 2004). XRD of the 4200 mm yr^{-1} subsurface samples (Fig. EA-3) indicate a clear pattern of reflections for a poorly-ordered kaolin-group mineral. Sorbed Fe^{2+} may also contribute to this peak, especially in the surface horizon, as Rancourt et al. (2005) have shown Fe^{2+} sorbed to bacterial cells can yield H_L lines even above 2.8 mm yr^{-1}. The H_L line at 2.18 mm s^{-1} matches well with pyroxene, but at this stage of weathering pyroxene is usually removed from the soil. We are the least confident of this ferrous assignment, although still highly confident that it is indeed a ferrous solid-phase.

4.4. Fe^{III}-oxides

Strong hematite XRD reflections (Figs. EA-2 and EA-3) in the lower rainfall soils provide a strong-basis for assigning the wide RT Fe^{III}-oxide sextets to hematite. The overall lower hyperfine fields (H_{peak}) of the MCG sextets than reference microcrystalline hematite (Fig. 5a) is consistent with smaller particle size (Dang et al., 1998) and/or cation substitution of Al or Ti within the Hm lattice (Degrave et al., 1988). However, the mass-specific magnetic susceptibility (MS) for these soils (χ up to 3.7×10^{-5} m^3 kg^{-1}) is much higher than expected for the antiferromagnetic (AFM) and superparamagnetic (SP) Fe^{III} phases Hm, Gt and Fh (Table 2), which typically have χ values of $\sim 5.0 \times 10^{-7}$ m^3 kg^{-1}. This strongly suggests ferrimagnetic solid-phases, such are magnetite or maghemite are present in these soils—although we note recent reports of a ferrimagnetic ferrihydrite (Michel et al., 2010) that may be applicable here as well. Typical χ values for magnetite or maghemite are $\sim 4.5 \times 10^{-4}$ m^3 kg^{-1}, so even trace amounts can significantly alter the bulk χ value for the soil. In the MCG soils, a strong correlation between MS and the mass of Fe^{III}-oxides (Fig. 6) suggests a ferrimagnetic solid-phase contributes to the Fe^{III}-Ox spectral area. Since, no magnetite octets were observed in any of the MBS spectra, and we have XRD and MBS evidence for maghemite (Mh) in some of the samples (e.g., Figs. 5, EA-2, and EA-3), a common

presence of Mh in these soils is more likely. If we assume all the MS in these soils results from Mh, we can estimate the mass of Mh using a typical χ value of 4.0×10^{-4} m^3 kg^{-1} Mh. By dividing this by the mass of Fe-oxides from the MBS spectra area (Table 3), we can roughly estimate the Mh contribution to the Fe-oxide fraction (Table EA-8 of the Electronic Annex). Comparing these values to the presence of either Hm or Mh related XRD peaks and the quadrapole splitting of the RT-Ox spectral component provides an interesting look at the Fe-oxides in these soils (Table EA-8 of the Electronic Annex). The Bhf values for Hm and Mh are very similar, but the two minerals have quite different ε values (Murad and Cashion, 2004) with $\varepsilon_{mc\text{-}Hm} \sim -0.10$ mm s^{-1} and $\varepsilon_{Mh} \sim -0.01$ mm s^{-1}. In the two deepest samples at the 3500 mm yr^{-1} site, the estimated Mh mass matches or exceeds the mass of MBS-assigned Fe-oxides, and these samples have ε values closest to zero. In the other samples, the Mh fraction of the Fe-oxide mass ranges from 0.1 to 0.7 with ε values between -0.08 and -0.13 mm s^{-1}. XRD peaks were generally observed when estimated concentrations of Hm or Mh were above $\sim$10 g Fe kg^{-1} soil. Thus, hematite likely represents the majority of Fe^{III}-Ox site populations (Figs. 2 and 3) with a sizable contribution of maghemite in the surface horizons and at depth in the 3500 mm yr^{-1} site. More detailed studies of the bulk magnetic properties of these soils are currently underway.

5. DISCUSSION

Fresh Hawaiian basalt has $\sim$86 g kg^{-1} Fe primarily in divalent form residing in pyroxenes, olivine, ilmenite and basaltic glass (Burkhard, 2001). Initial weathering of volcanic glass proceeds rapidly (Shoji et al., 1993), releasing Fe and Al and Si faster than crystalline minerals can precipitate, leading to soil solutions that are over-saturated with respect to several nanocrystalline or short-range-ordered phases (allophane, ferrihydrite, and opaline silica). These metastable solids have smaller critical nuclei and are favoured initially over more crystalline forms (Steefel and Van Cappellen, 1990). As weathering proceeds and the volcanic glass fraction is removed, soil solution activities of Fe, Al and Si are decreased. Further transformations of these SRO phases to crystalline minerals (e.g., kaolinite, gibbsite, goethite, hematite or quartz) depend strongly on environmental conditions and aging time. Our interpretation of MCG soils assumes nearly all of the primary ferrous iron was oxidized during early weathering stages (<20 ky). Therefore, our interpretation of the present-day Fe-phase variation, including the large decrease in total Fe across the MCG is the result of pedogenic forces acting on oxidized basalt transformation products.

5.1. Impact of increasing rainfall of Fe solid-phases

While increasing rainfall from 2800 to 4200 mm y^{-1} results in a proportional decrease in the soil Fe^{III}-(oxy)hydroxide $f_{tot\text{-}Fe}$, the ordering-temperature based subdivision of the Fe^{III}-OxHy class suggests that the mean particle size/crystallinity decreases (Fig. 2). This observation of a proportional *increase* of the most reactive and least crystalline Fe^{III}-OxHy components with increasing rainfall (and Fe removal via leaching) is unexpected. The conventional kinetic expectation in a dissolution-dominated environment (Sposito, 2008) is for the most reactive, soluble, and disordered (nanocrystalline) Fe solid-phases to be dissolved preferentially, resulting in selective retention of more kinetically stable, larger crystalline iron minerals, such as hematite (Stucki et al., 2007) and "bulk", large-crystalline goethite (Jones et al., 2009; Postma, 1993). We observe the opposite. Labile phases such as the nano Fe^{III}-(oxy)hydroxides (Fe^{III}-$OxHy_{(<4.2\ K)}$) maintain or increase their $f_{tot\text{-}Fe}$ abundance at higher rainfall sites (Fig. 4) while predictably recalcitrant phases such as Fe^{III}-Ox and Fe^{III}-$OxHy_{(>295\ K)}$ that are magnetically ordered at 295 K decrease as a $f_{tot\text{-}Fe}$. This is particularly true for the surface soils, which have a greater abundance of OM than the subsurface soils (Table 2).

5.2. Controls on Fe solid-phase composition

Evidently, Fe solid-phase transformations occur concurrently with significant Fe loss (Fig. 1) across the gradient. We suggest that the observed Fe species distribution across the gradient emerges because of a dynamic interplay between fluctuating redox conditions and the presence of cations and organic matter that alter the classic Ostwald ripening sequence (Ostwald, 1900). Mean Eh values for measurements logged weekly over a year illustrate sufficient Eh swings at all sites for both Fe reduction and re-oxidation of the released Fe^{2+}(aq) (Schuur and Matson, 2001) The sorption of Fe^{2+}(aq) onto Fe solid-phases has been shown to greatly accelerate mineral transformations that increase crystallinity via a process referred to as "atom exchange" (Charlet et al., 1998; Elsner et al., 2004; Fredrickson et al., 2004; Williams and Scherer, 2004; Crosby et al., 2005; Hansel et al., 2005; Pedersen et al., 2005; Larese-Casanova and Scherer, 2007; Gehin et al., 2007; Yanina and Rosso, 2008; Mikutta et al., 2009a). In fact, laboratory incubations with soils from this gradient indicate that oscillating redox conditions can produce large Fe^{2+}(aq) fluctuations that are superimposed on an overall increase in iron solid-phase crystallinity even on the time scale of weeks (Thompson et al., 2006b). Yet, low crystallinity Fe solids are abundant in these soils. We suggest this preservation of SRO solids is due to: (1) an open-system leaching environment that modulates the rise of Fe^{2+}(aq) concentrations during Fe reduction events and (2) the prevalence of organic matter (Table 2) in the surface horizons and Si and Ti in the subsurface horizons (Scribner et al., 2006) that retard the re-crystallization process. Retardation of Fe solid-phase transformation is well known to occur as a result of surface sorption of organic matter and Si, among other constituents (Schwertmann, 1966; Eusterhues et al., 2008; Mikutta et al., 2008; Jones et al., 2009). In fact, Jones et al. (2009) observed that the effects of Fe^{2+}-promoted atom exchange on Si-substituted ferrihydrite are different than on pure un-substituted Fh. Instead of the complete transformation to goethite observed for pure Fh, Fe^{2+} atom exchange on Si-substituted Fh preserves the Fh-structure, promoting Si release and the re-crystallization of

Si-free Fh particles. We hypothesize that this atom-exchange phenomenon also takes place in the MCG soils—which are intermittently exposed to Fe^{2+}(aq)—and likely exerts a pedogenic influence on the Fe solid-phase composition. We suggest that the resulting Fe solid-phase composition evolves in a leaching environment with consistent reductive dissolution forcing, intermittent oxidative-precipitation conditions, and processes that both accelerate (i.e., the presence of Fe^{2+}(aq)) and retard (i.e., the presence of sorbed OM and co-precipitated cations) solid-phase ripening.

5.3. Characteristics of short-range-ordered Fe on the MCG

Prior Fe solid-phase composition work in Hawaii has demonstrated these soils to be replete with short-range-ordered (SRO) or nanocrystalline Fe-solid-phases (Wada and Wada, 1976; Parfitt and Childs, 1988; Parfitt et al., 1988). Routinely, these SRO Fe phases are classified as ferrihydrite on the basis of selective extraction data, broad XRD peaks, or MBS at 77 K. With the exception of our previous work on the surface 3,500 mm yr^{-1} site (Thompson et al., 2006b), the only prior low temperature (<77 K) MBS measurements on Hawaiian soils were on relatively young, dry, soils weathered via palagonitic or solfataric processes near the mouth of volcanoes that serve as Martian soil analogs (Bishop et al., 2007). Only at very low temperatures (e.g., 4.2 K) can one use MBS to distinguish between paramagnetic silicate/organic bound Fe and superparamagnetic Fe^{III}-(oxy)hydroxides such as ferrihydrite and nano-goethite (Stucki et al., 2007). While our data do provide some marginal MBS and XRD evidence for the presence of ferrihydrite *sensu stricto* in some samples (e.g., Fig. 5), the majority of SRO Fe-(oxy)hydroxides in these soils are better approximated by synthetic nano-goethites (e.g., Van Der Zee et al., 2003). In most precise terms, the SRO Fe phases in these soils carry no known synthetic analog, but can likely be accurately represented as Fe^{III}-(oxy)hydroxides with nm particle sizes, high degrees of cation or OM substitution and/or other chemical/structural defects that decrease crystallinity.

This is especially true for the most disordered Fe^{III}-OxHy solids, which produces a collapsed sextet at LHT (LHT-(b)OxHy) indicative of dynamic or homogeneous line-broadening of an Fe phase near its ordering temperature (T_N). Such solid-phases must have much lower crystallinity and/or much smaller magnetic domain sizes than currently studied synthetic analogs of authigenic Fe^{III}-(oxy)hydroxides (e.g., ferrihydrite or nano-goethite with various degrees of cation substitution)—all of which, to our knowledge, are magnetically ordered at 4.2 K. A notable exception to this may be the DOM-Fe precipitate recently produced by Schwertmann et al. (2005), which in addition to an ordered Fh sextet, also includes a collapsed sextet feature at 4.2 K similar to our LHT-(b)OxHy sextet.

The association of Fe and organic matter may play an important role in determining the degree of disorder in soil Fe phases. Several recent studies have highlighted the effects of various organic components, organic matter and organic coatings on the magnetic properties of ferrihydrite (Schwertmann and Murad, 1988; Schwertmann et al., 2005; Eusterhues et al., 2008; Mikutta et al., 2008; Berquo et al., 2009; Michel et al., 2010). These studies illustrate that different carbon sources impact the Fh structure more substantially than others (Mikutta et al., 2008) decreasing Bhf between 1 and 3.5 T (Schwertmann et al., 2005; Eusterhues et al., 2008) and decreasing ordering temperature (T_N) up to 18 K. Even when changes to the Fh structure were minimal, Mikutta et al. (2008) found dramatic changes in the point of zero charge, surface area and mineral porosity for organic-Fh co-precipitates. However, when organic-compounds are surface-adsorbed rather than co-precipitated, reductions in Fh Bhf are minimal (Berquo et al., 2009). Since cation substitution (Goodman and Lewis, 1981; Degrave et al., 1988; Vandenberghe et al., 2000; Rancourt, 2001), small particle size, and lattice-defects can all substantially decrease T_N individually, it is easy to see how precipitates formed in the multi-component soil environment would give rise to even greater suppression of T_N, to near or below 4.2 K as observed in the MCG soils.

These SRO Fe phases (Fe^{III}-$OxHy_{(4.2–295\ K)}$ and Fe^{III}-$OxHy_{(4.2\ K)}$) comprise a large majority of the Fe in these soils and are likely representative of the SRO components commonly cited as the reactive Fe in intermediate-aged Hawaiian soils (Crews et al., 1995; Kitayama et al., 1997; Torn et al., 1997; Vitousek et al., 1997; Chorover et al., 1999, 2004; Chadwick and Chorover, 2001; Miller et al., 2001; Chadwick et al., 2003; Mikutta et al., 2009b, 2010).

5.4. Comparison of selective wet-chemical extractions and MBS phases

There is good correlation (Fig. 7) between the AAO extraction and the MBS-assigned nano Fe^{III}-(oxy)hydroxide phase (Fe-$OxHy_{(4.2\ K)}$, Table 3), but no apparent correlations between the MBS Fe site assignments and other selective extractions (Table 3). The concentrations of Fe extracted by Na-pyrophosphate are much larger than the MBS-assigned Fe silicate/organic phases, which would contain any Fe-coordinated with organic functionalities. In all but three samples from the wettest end of the gradient the moles of Fe extracted exceed estimates of the total ionisable surface functional groups on the organic matter (data not shown) assuming a mean 2 $mol_c\ kg^{-1}$ soil carbon (Essington, 2004). This suggests that most of the Na-pyrophosphate extractable Fe in these soils resides in nanocrystalline Fe^{III}-(oxy)hydroxides (Fe^{III}-$OxHy_{(4.2–295\ K)}$ and Fe^{III}-$OxHy_{(4.2\ K)}$), which are likely embedded in the organic matrix as observed previously (Chorover et al., 2004; Thompson et al., 2006a). The principal action of Na-pyrophosphate is to disperse aggregates of soil organic matter. When such a treatment is applied to volcanic soils with a high abundance of nano-sized mineral particles, these materials are measured along with the dispersed organic matter. Our observations are consistent those of Parfitt and Childs (1988) for a broader series of soils. It appears that in many cases Fe extracted by a standard Na-pyrophosphate extract does not resemble monomeric Fe-organic complexes, but rather includes nanocrystalline

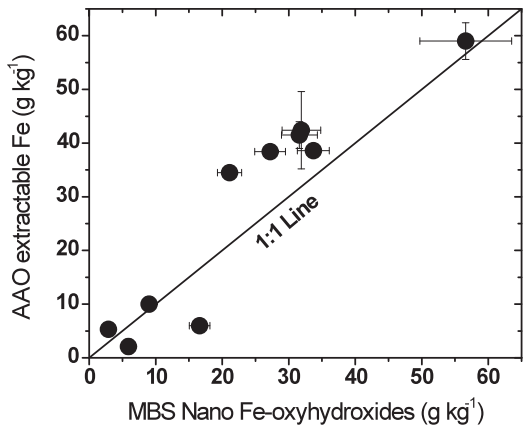

Fig. 7. Acid ammonium oxalate (AAO) extractable Fe vs. nano Fe^{III}-(oxy)hydroxide concentration calculated from the spectral area of the LHT-(b)OxHy for all soil samples (see Tables 2 and 3). The diagonal line indicates 1:1 correspondence between the variables.

Fe components. In addition, we obtained lower Fe recovery from CBD extractions than from Li-metaborate fusion (Table 2). This is consistent with prior observations by Parfitt et al. (1988), who found that some Hawaiian soil Fe-oxides were resistant to even multiple sequential CBD extractions, and Morris et al. (1993), who found hematite present in the CBD extract residue of Hawaiian palagonitic soils. These researchers attributed the apparent Fe phase recalcitrance to physical protection by a silicate matrix or large mineral particle sizes. We add that it could also be due to Fe co-precipitation.

5.5. Lack of significant solid-phase ferrous iron

The MCG soils do not contain significant quantities of ferrous iron despite low average Eh values in the wetter sites (Fig. 1). There is always a potential for Fe^{II} oxidation during sampling, transport and freeze-drying, but we were careful to N_2-flush the samples immediately after sampling and to open them only in a N_2/H_2 glove box until after they had been frozen at 193 K and freeze-dried. Hence, we believe low solid-phase ferrous abundances are a common feature of these variable-redox upland soils largely for two reasons: (1) low pH (<5) and low S and P content coupled with high leaching rates precludes solution oversaturation with respect to many common ferrous minerals (pyrite, siderite, vivianite, magnetite, green-rust); and (2) frequent fluctuations in dioxygen content (Fig. 1) that can rapidly oxidize ferrous to re-generate ferric iron phases. The combination of dynamic redox conditions and a high leaching rate likely separate these redox-affected upland soils from other redox-altered soils, such as those with fluctuating groundwater or soils in swales or wetlands.

6. CONCLUSION

The iron solid-phase composition along the Maui climate gradient develops within a context of leaching and dynamic redox conditions that vary as a function of rainfall. This results in extensive depletion of Fe with increasing rainfall. Concurrent with Fe depletion, is a coherent decrease in the fraction of total Fe ($f_{tot\text{-}Fe}$) assigned to Fe-(oxy)hydroxide phases and corresponding increases in the $f_{tot\text{-}Fe}$ of silicate/organic Fe and ferrous Fe phases. Interestingly, the crystallinity of the Fe-(oxy)hydroxide phases *decreases* with increasing rainfall, suggesting that organic matter (OM) co-precipitation and cation substitutions retard mineral ripening.

Across all sites, most of the Fe was present as a continuum of Fe^{III}-(oxy)hydroxides. Those at the more crystalline end are recognized as microcrystalline-goethites on the basis of both MBS and XRD, progressively less crystalline components are still best described as goethite, in this case nano-goethites (Van Der Zee et al., 2003), but with MBS properties that in some soils suggest an admixture with ferrihydrite or at least enough structural disorder to partially remove the axial asymmetry that characterizes the crystal structure of the needle-forming goethite mineral. The least crystalline end-members are highly disordered with blocking or Néel temperatures (T_N) suppressed near or below 4.2 K and are difficult to assign to goethite or ferrihydrite *senso stricto,* but rather can be most appropriately described as nano-Fe^{III}-(oxy)hydroxides. The latter end-members suggest extremely low-crystallinity arising from substitutional and other defects and/or from nanometric particle or coherent-ordering domain sizes. In this regard, our results are consistent with previous statements by Murad and Schwertmann (1980), who write:

> as particle sizes decrease the individual characteristics of the different iron oxides [and (oxy)hydroxides] gradually disappear, until finally only fundamental structural elements of short-range-order common to all, i.e., Fe^{3+} surrounded by six O, OH, and/or OH_2, remain. (p. 1048)

We would, however, broaden the statement to include substitutional and other defects affecting crystallinity, in addition to particle size (Rancourt et al., 2001, 2005; Thibault et al., 2009).

Our work suggests a need for future study on more appropriate synthetic analogs of co-precipitated Fe^{III}-(oxy)hydroxide solid phases. These reference solids would need to be co-precipitated with various cations and simple OM components under different precipitation kinetics to accumulate a broader range of nanocrystalline phases with low magnetic ordering temperatures. Such work, which is just beginning (e.g., Eusterhues et al., 2008; Mikutta et al., 2008; Thibault et al., 2009), is needed to further extend the interpretive power of Mössbauer spectroscopy.

ACKNOWLEDGMENTS

We thank Peter Vitousek for his leadership on the Hawaii Ecosystems Project, Heraldo Ferrington for logistical and sampling assistance in the field, Craig Rasmussen and Sarah Hayes for supporting XRD analysis and assistance, Ted Schuur for providing raw field Eh and pH data, Dr. Christoph Geiss (Trincoll Univeristy) for cross-calibrating our magnetic susceptibility measurements, and Dr. Mei-Zhen Dang (University of Ottawa) for supervising the cryogenic Mössbauer measurements. We also thank the two anonymous reviewers whose comments significantly improved this

manuscript. Funding was provided by the United States Department of Agriculture (USDA), Soil Processes Program NRI (2003-35107-13663) and AFRI Grants (2009-65107-05830), the National Science Foundation (NSF), the Natural Sciences and Engineering Research Council of Canada (NSERC), and the Andrew Mellon Foundation.

APPENDIX A. SUPPLEMENTARY DATA

Supplementary data associated with this article can be found, in the online version, at doi:10.1016/j.gca.2010.10.005.

REFERENCES

Bartlett R. J. and James B. R. (1993) Redox chemistry of soils. *Adv. Agron.* **50**, 151–208.

Berquo T. S., Erbs J. J., Lindquist A., Penn R. L. and Banerjee S. K. (2009) Effects of magnetic interactions in antiferromagnetic ferrihydrite particles. *J. Phys. Condes. Matter* **21**, 1–8.

Bishop J. L., Schiffman P., Murad E., Dyar M. D., Drief A. and Lane M. D. (2007) Characterization of alteration products in tephra from Haleakala, Maui: A visible-infrared spectroscopy, Mössbauer spectroscopy, XRD, EMPA and TEM study. *Clay Clay Miner.* **55**, 1–17.

Blum J. D., Klaue A., Nezat C. A., Driscoll C. T., Johnson C. E., Siccama T. G., Eagar C., Fahey T. J. and Likens G. E. (2002) Mycorrhizal weathering of apatite as an important calcium source in base-poor forest ecosystems. *Nature* **417**, 729–731.

Bonneville S., Van Cappellen P. and Behrends T. (2004) Microbial reduction of iron(III) oxyhydroxides: effects of mineral solubility and availability. *Chem. Geol.* **212**, 255–268.

Burkhard D. J. M. (2001) Crystallization and oxidation of Kilauea basalt glass: processes during reheating experiments. *J. Petrol.* **42**, 507–527.

Chadwick O. A. and Chorover J. (2001) The chemistry of pedogenic thresholds. *Geoderma* **100**, 321–353.

Chadwick O. A., Gavenda R. T., Kelly E. F., Ziegler K., Olson C. G., Elliott W. C. and Hendricks D. M. (2003) The impact of climate on the biogeochemical functioning of volcanic soils. *Chem. Geol.* **202**, 195–223.

Charlet L., Liger E. and Gerasimo P. (1998) Decontamination of TCE- and U-rich waters by granular iron: role of sorbed Fe(II). *J. Environ. Eng. ASCE* **124**, 25–30.

Chorover J., Amistadi M. K. and Chadwick O. A. (2004) Surface charge evolution of mineral–organic complexes during pedogenesis in Hawaiian basalt. *Geochim. Cosmochim. Acta* **68**, 4859–4876.

Chorover J., DiChiaro M. J. and Chadwick O. A. (1999) Structural charge and cesium retention in a chronosequence of tephritic soils. *Soil Sci. Soc. Am. J.* **63**, 169–177.

Cornell R. M. and Schwertmann U. (2003) The iron oxides: characterization (ch. 7). In *The Iron Oxides* (eds. R. M. Cornell and U. Schwertmann). VCH, New York, NY.

Crews T. E., Kitayama K., Fownes J. H., Riley R. H., Herbert D. A., Muellerdombois D. and Vitousek P. M. (1995) Changes in soil-phosphorus fractions and ecosystem dynamics across a long chronosequence in Hawaii. *Ecology* **76**, 1407–1424.

Crosby H. A., Johnson C. M., Roden E. E. and Beard B. L. (2005) Coupled Fe(II)–Fe(III) electron and atom exchange as a mechanism for Fe isotope fractionation during dissimilatory iron oxide reduction. *Environ. Sci. Technol.* **39**, 6698–6704.

Dang M. Z., Rancourt D. G., Dutrizac J. E., Lamarche G. and Provencher R. (1998) Interplay of surface conditions, particle size, stoichiometry, cell parameters, and magnetism in synthetic hematite-like materials. *Hyperfine Interact.* **117**, 271–319.

Davidson E. A., Chorover J. and Dail D. B. (2003) A mechanism of abiotic immobilization of nitrate in forest ecosystems: the ferrous wheel hypothesis. *Global Change Biol.* **9**, 228–236.

Degrave E., Bowen L. H., Amarasiriwardena D. D. and Vandenberghe R. E. (1988) Fe-57 Mössbauer-effect study of highly substituted aluminum hematites–determination of the magnetic hyperfine field distributions. *J. Magn. Magn. Mater.* **72**, 129–140.

Derry L. A., Kurtz A. C., Ziegler K. and Chadwick O. A. (2005) Biological control of terrestrial silica cycling and export fluxes to watersheds. *Nature* **433**, 728–731.

Elsner M., Schwarzenbach R. P. and Haderlein S. B. (2004) Reactivity of Fe(II)-bearing minerals toward reductive transformation of organic contaminants. *Environ. Sci. Technol.* **38**, 799–807.

Essington M. E. (2004) *Soil and Water Chemistry: An Integrative Approach*. CRC Press Inc., New York, NY.

Eusterhues K., Wagner F. E., Häusler W., Hanzlik M., Knicker H., Totsche K. U., Kögel-Knabner I. and Schwertmann U. (2008) Characterization of ferrihydrite-soil organic matter coprecipitates by X-ray diffraction and Mössbauer spectroscopy. *Environ. Sci. Technol.* **42**, 7891–7897.

Fey M. V. and Dixon J. B. (1981) Synthesis and properties of poorly crystalline hydrated aluminous goethites. *Clay Clay Miner.* **29**, 91–100.

Fredrickson J. K., Zachara J. M., Kennedy D. W., Kukkadapu R. K., McKinley J. P., Heald S. M., Liu C. X. and Plymale A. E. (2004) Reduction of TcO4- by sediment-associated biogenic Fe(II). *Geochim. Cosmochim. Acta* **68**, 3171–3187.

Fritsch E., Morin G., Bedidi A., Bonnin D., Balan E., Caquineau S. and Calas G. (2005) Transformation of haematite and Al-poor goethite to Al-rich goethite and associated yellowing in a ferralitic clay soil profile of the middle Amazon Basin (Manaus, Brazil). *Eur. J. Soil Sci.* **56**, 575–588.

Fysh S. A., Cashion J. D. and Clark P. E. (1983) Mössbauer-effect studies of iron in kaoline: 1. Structural iron. *Clay Clay Miner.* **31**, 285–292.

Gehin A., Greneche J. M., Tournassat C., Brendle J., Rancourt D. G. and Charlet L. (2007) Reversible surface-sorption-induced electron-transfer oxidation of Fe(II) at reactive sites on a synthetic clay mineral. *Geochim. Cosmochim. Acta* **71**, 863.

Genin J. M. R., Refait P., Bourrie G., Abdelmoula M. and Trolard F. (2001) Structure and stability of the Fe(II)–Fe(III) green rust "fougerite" mineral and its potential for reducing pollutants in soil solutions. *Appl. Geochem.* **16**, 559–570.

Golden D. C., Bowen L. H., Weed S. B. and Bigham J. M. (1979) Mössbauer studies of synthetic and soil-occurring aluminum-substituted goethites. *Soil Sci. Soc. Am. J.* **43**, 802–808.

Goodman B. A. and Lewis D. G. (1981) Mössbauer-spectra of aluminous goethites (FeOOH). *J. Soil Sci.* **32**, 351–363.

Hansel C. M., Benner S. G. and Fendorf S. (2005) Competing Fe(II)-induced mineralization pathways of ferrihydrite. *Environ. Sci. Technol.* **39**, 7147–7153.

Jones A. M., Collins R. N., Rose J. and Waite T. D. (2009) The effect of silica and natural organic matter on the Fe(II)-catalysed transformation and reactivity of Fe(III) minerals. *Geochim. Cosmochim. Acta* **73**, 4409–4422.

Kitayama K., Schuur E. A. G., Drake D. R. and Muellerdombois D. (1997) Fate of a wet montane forest during soil ageing in Hawaii. *J. Ecol.* **85**, 669–679.

Kukkadapu R. K., Zachara J. M., Smith S. C., Fredrickson J. K. and Liu C. X. (2001) Dissimilatory bacterial reduction of Al-substituted goethite in subsurface sediments. *Geochim. Cosmochim. Acta* **65**, 2913–2924.

Lalonde A. E., Rancourt D. G. and Ping J. Y. (1998) Accuracy of ferric/ferrous determinations in micas: a comparison of Mössbauer spectroscopy and the Pratt and Wilson wet-chemical methods. *Hyperfine Interact.* **117**, 175–204.

Langmuir D. (1971) Particle size effect on reaction: goethite = hematite + water. *Am. J. Sci.* **271**, 147–156.

Larese-Casanova P. and Scherer M. M. (2007) Fe(II) sorption on hematite: new insights based on spectroscopic measurements. *Environ. Sci. Technol.* **41**, 471–477.

Loeppert R. H. and Inskeep W. P. (1996) Iron. In *Methods of Soil Analysis: Part 3 – Chemical Methods* (ed. D. L. Sparks). Soil Science Society of America.

Lucas Y., Luizao F. J., Chauvel A., Rouiller J. and Nahon D. (1993) The relation between biological-activity of the rain-forest and mineral-composition of soils. *Science* **260**, 521–523.

Marchand P. and Rancourt D. G. (2009) General model for the aqueous precipitation of rough-surface nanocrystals and application to ferrihydrite genesis. *Am. Mineral.* **94**, 1428–1439.

Michel F. M., Barron V., Torrent J., Morales M. P., Serna C. J., Boily J. F., Liu Q. S., Ambrosini A., Cismasu A. C. and Brown G. E. (2010) Ordered ferrimagnetic form of ferrihydrite reveals links among structure, composition, and magnetism. *Proc. Natl. Acad. Sci. USA* **107**, 2787–2792.

Mikutta C., Mikutta R., Bonneville S., Wagner F., Voegelin A., Christl I. and Kretzschmar R. (2008) Synthetic coprecipitates of exopolysaccharides and ferrihydrite. Part I: characterization. *Geochim. Cosmochim. Acta* **72**, 1111–1127.

Mikutta C., Wiederhold J. G., Cirpka O. A., Hofstetter T. B., Bourdon B. and Von Gunten U. (2009a) Iron isotope fractionation and atom exchange during sorption of ferrous iron to mineral surfaces. *Geochim. Cosmochim. Acta* **73**, 1795–1812.

Mikutta R., Kaiser K., Dörr N., Vollmer A., Chadwick O. A., Chorover J., Kramer M. G. and Guggenberger G. (2010) Mineralogical impact on organic nitrogen across a long-term soil chronosequence (0.3–4100 kyr). *Geochim. Cosmochim. Acta* **74**, 2142–2164.

Mikutta R., Schaumann G. E., Gildemeister D., Bonneville S., Kramer M. G., Chorover J., Chadwick O. A. and Guggenberger G. (2009b) Biogeochemistry of mineral–organic associations across a long-term mineralogical soil gradient (0.3–4100 kyr), Hawaiian Islands. *Geochim. Cosmochim. Acta* **73**, 2034–2060.

Miller A. J., Schuur E. A. G. and Chadwick O. A. (2001) Redox control of phosphorus pools in Hawaiian montane forest soils. *Geoderma* **102**, 219–237.

Morris R. V., Golden D. C., Bell J. F., Lauer H. V. and Adams J. B. (1993) Pigmenting agents in martian soils – inferences from spectral, Mössbauer, and magnetic-properties of nanophase and other iron-oxides in Hawaiian palagonitic soil Pn-9. *Geochim. Cosmochim. Acta* **57**, 4597–4609.

Murad E. and Cashion J. (2004) *Mössbauer Spectroscopy of Environmental Materials and their Industrial Utilization*. Kluwer Academic Publishers Group, Norwell, Massachusetts.

Murad E. and Schwertmann U. (1980) The Mössbauer spectrum of ferrihydrite and its relations to those of other iron-oxides. *Am. Mineral.* **65**, 1044–1049.

Murad E. and Schwertmann U. (1983) The influence of aluminum substitution and crystallinity on the Mössbauer-spectra of goethite. *Clay Miner.* **18**, 301–312.

Norrish K. and Taylor R. M. (1961) Isomorphous replacement of iron by aluminium in soil goethites. *J. Soil Sci.* **12**, 294.

Ostwald W. (1900) On the assumed isomerism of red and yellow mercury oxide and the surface-tension of solid bodies. *Z. Phys. Chem. Stoch. Ve.* **34**, 495–503.

Otero X. L., Ferreira T. O., Huerta-Diaz M. A., Partiti C. S. M., Souza V., Vidal-Torrado P. and Macias F. (2009) Geochemistry of iron and manganese in soils and sediments of a mangrove system, Island of Pai Matos (Cananeia – SP, Brazil). *Geoderma* **148**, 318–335.

Parfitt R. L. and Childs C. W. (1988) Estimation of forms of Fe and Al – a review, and analysis of contrasting soils by dissolution and Mössbauer methods. *Aus. J. Soil Res.* **26**, 121–144.

Parfitt R. L., Childs C. W. and Eden D. N. (1988) Ferrihydrite and allophane in four Andepts from Hawaii and implications for their classification. *Geoderma* **41**, 223–241.

Pedersen H. D., Postma D., Jakobsen R. and Larsen O. (2005) Fast transformation of iron oxyhydroxides by the catalytic action of aqueous Fe(II). *Geochim. Cosmochim. Acta* **69**, 3967–3977.

Postma D. (1993) The reactivity of iron-oxides in sediments: a kinetic approach. *Geochim. Cosmochim. Acta* **57**, 5027–5034.

Rancourt D. G. (1998) Mössbauer spectroscopy in clay science. *Hyperfine Interact.* **117**, 3–38.

Rancourt D. G. (2001) Magnetism of earth, planetary, and environmental nanomaterials. *Rev. Mineral. Geochem.* **44**, 217–292.

Rancourt D. G., Fortin D., Pichler T., Thibault P. J., Lamarche G., Morris R. V. and Mercier P. H. J. (2001) Mineralogy of a natural as-rich hydrous ferric oxide coprecipitate formed by mixing of hydrothermal fluid and seawater: implications regarding surface complexation and color banding in ferrihydrite deposits. *Am. Mineral.* **86**, 834–851.

Rancourt D. G., McDonald A. M., Lalonde A. E. and Ping J. Y. (1993) Mössbauer absorber thicknesses for accurate site populations in Fe-bearing minerals. *Am. Mineral.* **78**, 1–7.

Rancourt D. G. and Meunier J. F. (2008) Constraints on structural models of ferrihydrite as a nanocrystalline material. *Am. Mineral.* **93**, 1412–1417.

Rancourt D. G. and Ping J. Y. (1991) Voigt-based methods for arbitrary-shape static hyperfine parameter distributions in Mössbauer-spectroscopy. *Nucl. Instrum. Methods Phys. Res. Sect. B* **58**, 85–97.

Rancourt D. G., Thibault P.-J., Mavrocordatos D. and Lamarche G. (2005) Hydrous ferric oxide precipitation in the presence of nonmetabolizing bacteria: constraints on the mechanism of a biotic effect. *Geochim. Cosmochim. Acta* **69**, 553–577.

Roden E. E. (2006) Geochemical and microbiological controls on dissimilatory iron reduction. *C.R. Geosci.* **338**, 456–467.

Schuur E. A. G. and Matson P. A. (2001) Net primary productivity and nutrient cycling across a mesic to wet precipitation gradient in Hawaiian montane forest. *Oecologia* **128**, 431–442.

Schwertmann U. (1966) Inhibitory effect of soil organic matter on crystallization of amorphous ferric hydroxide. *Nature* **212**, 645–646.

Schwertmann U. and Murad E. (1988) The nature of an iron-oxide organic iron association in a peaty environment. *Clay Miner.* **23**, 291–299.

Schwertmann U., Wagner F. and Knicker H. (2005) Ferrihydrite-humic associations: magnetic hyperfine interactions. *Soil Sci. Soc. Am. J.* **69**, 1009–1015.

Scribner A. M., Kurtz A. C. and Chadwick O. A. (2006) Germanium sequestration by soil: targeting the roles of secondary clays and Fe-oxyhydroxides. *Earth Planet. Sci. Lett.* **243**, 760–770.

Sexstone A. J., Revsbech N. P., Parkin T. B. and Tiedje J. M. (1985) Direct measurement of oxygen profiles and denitrification rates in soil aggregates. *Soil Sci. Soc. Am. J.* **49**, 645–651.

Shoji S., Nanzyo M. and Dahlgren R. A. (1993) *Volcanic Ash Soils: Genesis, Properties and Utilization*. Elsevier, New York.

Sposito G. (2008) *The Chemistry of Soils*. Oxford University Press, New York.

Steefel C. I. and Van Cappellen P. (1990) A new kinetic approach to modeling water–rock interaction: the role of nucleation, precursors, and ostwald ripening. *Geochim. Cosmochim. Acta* **54**, 2657–2677.

Stucki J. W., Lee K., Goodman B. A. and Kostka J. E. (2007) Effects of in situ biostimulation on iron mineral speciation in a sub-surface soil. *Geochim. Cosmochim. Acta* **71**, 835–843.

Thibault P. J., Rancourt D. G., Evans R. J. and Dutrizac J. E. (2009) Mineralogical confirmation of a near-P:Fe = 1:2 limiting stoichiometric ratio in colloidal P-bearing ferrihydrite-like hydrous ferric oxide. *Geochim. Cosmochim. Acta* **73**, 364–376.

Thompson A., Chadwick O. A., Boman S. and Chorover J. (2006a) Colloid mobilization during soil iron redox oscillations. *Environ. Sci. Technol.* **40**, 5743–5749.

Thompson A., Chadwick O. A., Rancourt D. G. and Chorover J. (2006b) Iron-oxide crystallinity increases during soil redox oscillations. *Geochim. Cosmochim. Acta* **70**, 1710–1727.

Thompson A., Ruiz J., Chadwick O. A., Titus M. and Chorover J. (2007) Rayleigh fractionation of iron isotopes during pedogenesis along a climate sequence of Hawaiian basalt. *Chem. Geol.* **238**, 72–83.

Torn M. S., Trumbore S. E., Chadwick O. A., Vitousek P. M. and Hendricks D. M. (1997) Mineral control of soil organic carbon storage and turnover. *Nature* **389**, 170–173.

Van Der Zee C., Roberts D. R., Rancourt D. G. and Slomp C. P. (2003) Nanogoethite is the dominant reactive oxyhydroxide phase in lake and marine sediments. *Geology* **31**, 993–996.

Vandenberghe R. E., Barrero C. A., da Costa G. M., Van San E. and De Grave E. (2000) Mössbauer characterization of iron oxides and (oxy)hydroxides: the present state of the art. *Hyperfine Interact.* **126**, 247–259.

Vitousek P. M., Chadwick O. A., Crews T. E., Fownes J. H., Hendricks D. H. and Herbert D. (1997) Soil and ecosystem development across the Hawaiian islands. *GSA Today* **7**, 1–8.

Wada K. and Wada S.-I. (1976) Clay mineralogy of the B horizons of two hydrandepts, a Torrox and a Humitropept in Hawaii. *Geoderma* **16**, 139–157.

Waychunas G. A., Kim C. S. and Banfield J. F. (2005) Nanoparticulate iron oxide minerals in soils and sediments: unique properties and contaminant scavenging mechanisms. *J. Nanopart. Res.* **7**, 409–433.

Williams A. G. B. and Scherer M. M. (2004) Spectroscopic evidence for Fe(II)–Fe(III) electron transfer at the iron oxide–water interface. *Environ. Sci. Technol.* **38**, 4782–4790.

Yamaguchi K. E., Johnson C. M., Beard B. L. and Ohmoto H. (2005) Biogeochemical cycling of iron in the Archean-Paleoproterozoic Earth: constraints from iron isotope variations in sedimentary rocks from the Kaapvaal and Pilbara Cratons. *Chem. Geol.* **218**, 135–169.

Yanina S. V. and Rosso K. M. (2008) Linked reactivity at mineral–water interfaces through bulk crystal conduction. *Science* **320**, 218–222.

Associate editor: Donald L. Sparks